Journal of Engineering Mathematics (2006) 54: 181–196
DOI 10.1007/s10665-005-9014-1

Effect of near-critical swirl on the Burke-Schumann reaction sheet

KANG-HO SOHN, ZVI RUSAK and ASHWANI K. KAPILA
Rensselaer Polytechnic Institute, Troy, New York 12180-3590, U.S.A. (E-mail: kapila@rpi.edu)

Received 24 November 2004; accepted in revised form 1 August 2005 / Published online: 3 January 2006

Abstract. The influence of swirl on the shape of the Burke-Schumann reaction sheet in a straight cylindrical pipe is investigated by asymptotic and numerical means. Attention is confined to swirl levels that are near the critical value at which vortex breakdown occurs. A high-Reynolds-number, laminar, isothermal, low-Mach-number reacting flow is considered. An asymptotic analysis is developed to study the nonlinear interaction between near-critical swirl and mixture fraction distribution within the flow. It is first shown that leading-order perturbation of the velocity field from the columnar state, generated by the interaction of near-critical swirl and low viscosity, can be described by a nonlinear reduced-order model. This flow perturbation is computed, and then employed to determine the correction to the classical Burke-Schumann solution. Under lean conditions of reaction the reaction sheet becomes shorter and more compact as swirl is increased. For rich conditions of reaction, increasing swirl first causes the reaction-sheet length to decrease, and then increase after vortex breakdown has appeared. Numerical simulations of the flow and reaction-zone shape are substantiated by, and supplement, the asymptotic results.

Key words: Burke-Schumann reaction zone, diffusional combustion, near-criticality, swirling flow, vortex breakdown,

1. Introduction

The study of diffusive (non-premixed) combustion, which is deemed to be safer and more economical than premixed combustion, has a long history. The classical solution of Burke and Schumann [1] describes the steady structure, in terms of mixture fraction distribution, of the flame sheet that is produced when two co-axial jets of fuel and oxidizer are injected into a straight cylindrical pipe; see also Williams [2, Section 3.1]. The original Burke-Schumann formulation focused on the balance between streamwise convection and transverse diffusion of species by considering the species conservation equation alone. Constant axial velocity and infinite rate of reaction were assumed and effects of heat release due to chemical reaction, transverse convection resulting from thermal expansion effects, axial diffusion of species, and viscous dissipation were neglected. Despite these deviations from realism, the Burke-Schumann solution captured rather well the fundamental character of the diffusion flame, to the extent that it has served as the canonical model for illustrating the structure of diffusional combustion.

By adding energy conservation to species balance, Williams [2, Section 3.4], extended the Burke-Schumann approach to compute the steady-state fields of mixture fraction as well as temperature, for unit Lewis number (Le). Momentum equations were not considered in the analysis; in fact, these equations cannot be satisfied by the solutions of the mass fraction and energy equations. Roper [3] modified the Burke-Schumann theory to satisfy the continuity equation when velocity and temperature fields are not constant. Again, momentum equations were not considered. Roper predicted a small effect of the modifications on the flame size for a circular port burner. The experiments of Roper et al. [4] showed agreement with the flame length predicted by Roper's theory [3]. Klajan and Oppenhiem [5] developed an analytical approach to

describe the effect of exothermicity on the shape of jet diffusion flames and associated temperature and flow fields. They constructed self-similar solutions using the Dorodnitsyn-Howarth transformation of the compressible flow equations and found agreement of the flame length with experimental data under zero gravity conditions. Chung and Law [6] revised the Burke-Schumann formulation to include effects of streamwise as well as preferential diffusion of species and heat for flows with non-unity Lewis number. They used a perturbation analysis for flames at near-unity Le and described Lewis-number effects on flame shape and temperature at various Peclet numbers (Pe). Li, Gordon, and Williams [7] analyzed highly over-ventilated flames in an infinite atmosphere at Le = 1. They used the reaction sheet approximation and included buoyancy. A boundary-layer approximation in the stream-function coordinates was used to simplify numerical integration of the flow and species equations. The radial momentum equation was not considered. Computed results of the flame-length dependence on fuel flow rate for various hydrocarbon fuels showed agreement with experimental data.

Although in broad use, diffusional combustion is prone to instabilities, flame lift-off, and extinction [2, Section 10.2]. In recent years it has been found that exerting swirl on diffusion flames may help eliminate blowout, reduce flame lift-off distance, improve flame stability, and enhance combustion performance (see, for example, the experimental results in [8, Chapters 3 and 4], [9], [10, Chapter 13], [11], [12]). Typically, flows with combustion and high levels of swirl exhibit complex patterns, including large-scale internal separation (vortex breakdown) zones that create transverse convection, which in turn significantly affects flame length and shape. Analysis of this situation is challenging, and to the best of our knowledge there is no mathematical investigation of diffusive combustion with swirl. Current studies concentrate on extensive numerical simulations (see, for example, [13–16]).

This effort is a first step toward developing a better understanding of the effects of swirl on diffusion flames. It combines asymptotic analysis and numerical computation, and focuses on the influence of near-critical swirl and the first appearance of vortex breakdown on the Burke-Schumann flame structure. The flow is laminar and the Reynolds number is high, and the heat released by the chemical reaction is ignored. The last assumption is drastic in a combustion context, as it yields an isothermal reaction zone rather than a flame. However, it is made here by design, to isolate effects of swirl from those of thermal expansion. The approach can be extended to include effects of small exothermicity, as demonstrated in the context of premixed combustion by Rusak et al. [17]. Application to nonpremixed combustion, examined in Sohn's thesis [18], will be the subject of a forthcoming publication. Heat release of order unity, on the other hand, may well require a fully numerical treatment.

The asymptotic approach adopted here is based on Wang and Rusak's [19] treatment of cold, inert flows. These authors provide an asymptotic description of the flow disturbance generated by the interaction between swirl and viscosity. They show that large disturbances appear in the flow as the swirl level approaches a critical value ω_c, signifying the first occurrence of vortex breakdown. Their results agree well with numerically obtained Navier-Stokes solutions of Beran and Culick [20], Beran [21], and Lopez [22]. We employ Wang and Rusak's [19] asymptotic description of the flow to determine the effect of the flow on the shape of the reaction zone. The asymptotic predictions are numerically substantiated through extensive simulations of the flow field and the flame shape.

2. The mathematical model

We consider a pipe in the form of a right-circular cylinder with a finite length. Nonpremixed reactants, supplied as an inner stream of fuel surrounded by a coaxial outer stream

of oxidant, pass through a swirl generator placed upstream of the inlet prior to entering the chamber.

The mathematical formulation is based on several assumptions about the nature of the flow and the process of reaction. We consider the limit of zero heat release and low Mach number. Then, energy balance implies that the flow is isothermal, while the gas law leads to constant density. Following Burke-Schumann, we also consider infinitely fast chemistry so that the reaction is confined to a thin sheet. Transport coefficients such as thermal conductivity, viscosity and species diffusion coefficients are assumed constant. Then the non-dimensional equations of mass, momentum, energy and species balance for a steady, axi-symmetric, incompressible and viscous flow of a reactive fluid are:

$$\frac{1}{r}(ru)_r + w_x = 0, \tag{1}$$

$$uu_r + wu_x - x_0^2\frac{v^2}{r} = -x_0^2 p_r + \frac{x_0}{\mathrm{Re}}\left\{\left(\frac{1}{r}(ru)_r\right)_r + \frac{u_{xx}}{x_0^2}\right\}, \tag{2}$$

$$uv_r + \frac{uv}{r} + wv_x = \frac{x_0}{\mathrm{Re}}\left\{\left(\frac{1}{r}(rv)_r\right)_r + \frac{v_{xx}}{x_0^2}\right\}, \tag{3}$$

$$uw_r + ww_x = -p_x + \frac{x_0}{\mathrm{Re}}\left\{\frac{1}{r}(rw_r)_r + \frac{w_{xx}}{x_0^2}\right\}, \tag{4}$$

$$uf_r + wf_x = \frac{x_0}{\mathrm{Pe}}\left\{\frac{1}{r}(rf_r)_r + \frac{f_{xx}}{x_0^2}\right\}. \tag{5}$$

Here,

$$f = \frac{\nu Y_F - Y_O + Y_{O,0}}{\nu Y_{F,0} + Y_{O,0}}, \tag{6}$$

where

$$\nu = \frac{W_O(\nu_O'' - \nu_O')}{W_F(\nu_F'' - \nu_F')}. \tag{7}$$

The above nondimensionalization is based on the following reference quantities. The axial length scales with the pipe length $\hat{\ell}_0$ and the radial length with the pipe radius $\hat{r}_0$, with $x_0 = \hat{\ell}_0/\hat{r}_0$ being the length-to-radius ratio. The axial and circumferential speeds are scaled with the inlet axial speed $\hat{U}_0$ and the radial speed with $\hat{U}_0/x_0$. The speeds u, v and w are, respectively, the non-dimensional radial, circumferential, and axial components of the velocity, Y_F and Y_O denote the fuel and oxygen mass fractions respectively, and f is the mixture mass fraction, derived for example in [23, Chapter 1]. Also, W_F and W_O are the respective molecular weights of fuel and oxygen, ν_i' is the stoichiometric coefficient for species i appearing as a reactant and ν_i' that for species i appearing as a product, while ν is the stoichiometric oxygen-to-fuel mass ratio. The dimensionless parameters appearing above are the Reynolds number $\mathrm{Re} = \hat{\rho}_0\hat{U}_0\hat{r}_0/\hat{\mu}$, and the Peclet number $\mathrm{Pe} = \hat{\rho}_0\hat{U}_0\hat{r}_0/\hat{D}$. Here $\hat{p}_0$ and $\hat{\rho}_0$ are the reference values of pressure and density respectively, $\hat{\mu}$ is the viscosity, and $\hat{D}$ the mass diffusion coefficient for both fuel and oxidant (corresponding to a Lewis number of unity). The dimensionless pressure p appearing in the above equations is the pressure excess above the ambient value $\hat{p}_0 = \hat{\rho}_0\mathcal{R}\hat{T}_0$ in units of $\gamma M_0^2\hat{p}_0$, *i.e.*, $\hat{p} = \hat{p}_0(1 + \gamma M_0^2 p)$. Here $M_0 = \sqrt{\hat{U}_0^2/(\gamma\,\hat{p}_0/\hat{\rho}_0)}$ is the Mach number, γ the specific heats ratio, and $\hat{T}_0$ the reference (ambient) temperature.

We consider a sufficiently long, straight pipe and a large Reynolds number such that the following asymptotic ordering applies:

$$x_0 \gg 1, \quad \mathrm{Re} \gg 1, \quad \text{and} \quad 0 < \frac{x_0}{\mathrm{Re}} \ll 1.$$

Equations (1–5) show that the solution for the flow velocity is decoupled from the solution for the mixture fraction f. Specifically, the solution for f is determined after the solution for the velocity field has been found.

The flow is subject to the following boundary conditions. At the pipe inlet $x = 0$, axial and circumferential speeds and axial gradient of the radial speed are prescribed as

$$w(0, r) = w_0(r), \quad v(0, r) = \omega v_0(r), \quad u_x(0, r) = 0, \quad \text{for} \quad 0 \le r \le 1. \tag{8}$$

The above condition on u_x is equivalent to prescribing the azimuthal vorticity as $\eta(0, r) = w_0'(r)$, and provides the freedom necessary for the development of a radial velocity profile at the inlet to reflect the upstream influence of disturbances that have a tendency to cast such an influence. Here ω is the swirl ratio, representing the strength of the vortex flow. These inlet conditions are sufficiently general to model a swirling flow produced by a vortex generator located immediately upstream of the inlet and operating in a steady and continuous manner. These conditions also correspond to the cold and incompressible vortex flow experiments of Bruecker and Althaus [26], Malkiel *et al.* [27] and Mattner *et al.* [28]. In addition to (8) we assume that the inlet flow is a two-gas (fuel and oxidant) stream, with the two constituents separated at an inner radius $0 < R_i < 1$. The mixture mass fraction in each region is given by

$$\text{Fuel: } f(0, r) = 1 \quad \text{for} \quad 0 \le r < R_i; \qquad \text{Oxidant: } f(0, r) = 0 \quad \text{for} \quad R_i < r \le 1. \tag{9}$$

At the pipe outlet $x = 1$ it is assumed that the radial speed, the streamwise derivatives of the axial and circumferential speeds and the mixture mass fraction vanish, *i.e.*,

$$u(1, r) = v_x(1, r) = w_x(1, r) = 0, \quad f_x(1, r) = \text{e.s.t for } 0 \le r \le 1. \tag{10}$$

Here e.s.t. denotes an exponentially small term, in accordance with the Burke-Schumann solution and the expected columnar state at the outlet for $x_0 \gg 1$.

The pipe axis of symmetry is a streamline along which the radial and azimuthal velocity components vanish, as do the radial gradients of the axial velocity and mixture fraction. Consequently, we set

$$u(x, 0) = v(x, 0) = w_r(x, 0) = f_r(x, 0) = 0 \quad \text{for} \quad 0 \le x \le 1. \tag{11}$$

Only the impermeability, but not the no-slip, condition is enforced along the wall $r = 1$. This condition ignores the influence of wall boundary layers, with the expectation that these layers exert at most a quantitative effect on the phenomenon under study; see for example, the relevant discussion in [20] and [22]. Also, along the pipe wall, the radial gradient of the mixture mass fraction vanishes. Thus we have

$$u(x, 1) = f_r(x, 1) = 0 \quad \text{for} \quad 0 \le x \le 1. \tag{12}$$

By virtue of axisymmetry (*i.e.*, the absence of azimuthal derivatives in the governing equations and boundary conditions) and the continuity equation (1), a stream function ψ can be defined where the radial component of velocity $u = -\psi_x / r$ and the axial component $w = \psi_r / r$. Let a new radial coordinate y be defined by $y = r^2/2$. Then, $u = -\psi(x, y)_x / \sqrt{2y}$, $w = \psi_y(x, y)$,

and the azimuthal vorticity $\eta = r\chi$ where $\chi \equiv -\{\psi_{yy} + \psi_{xx}/(2x_0^2 y)\}$. Along the inlet we have $\psi_0(y) \equiv \psi(0, y)$, with $\psi_{0_y} = w_0(y)$ and $\chi_0(y) \equiv \chi(0, y) = -w_{0_y}$. It is also convenient to define the circulation $K(x, y)$ by $K \equiv rv$. Then, at the inlet, $K_0(y) \equiv K(0, y) = \omega r v_0(r)$. The following equations can now be derived from the set (1–5):

$$\psi_y K_x - \psi_x K_y = \frac{2x_0}{\mathrm{Re}}\, y \left(K_{yy} + \frac{1}{2x_0^2}\frac{K_{xx}}{y} \right), \tag{13}$$

$$\psi_y \chi_x - \psi_x \chi_y = \frac{(K^2)_x}{4y^2} + \frac{2x_0}{\mathrm{Re}} \left\{ y \left(\chi_{yy} + \frac{1}{2x_0^2}\frac{\chi_{xx}}{y} \right) + 2\chi_y \right\}, \tag{14}$$

$$\psi_y f_x - \psi_x f_y = \frac{x_0}{\mathrm{Pe}} \left((2y f_y)_y + \frac{f_{xx}}{x_0^2} \right). \tag{15}$$

Note that pressure is eliminated from the problem by cross-differentiation of (2) and (4) and by the introduction of χ. The boundary conditions (8–12) transform into

$$\begin{aligned} \psi(x, 0) = 0,\ \psi(x, 1/2) = \psi_0(1/2),\ \sqrt{y} f_y(x, 0) = f_y(x, 1/2) = 0 \quad & \text{for } 0 \le x \le 1, \\ \psi(0, y) = \psi_0(y),\ \psi_{xx}(0, y) = 0,\ K(0, y) = K_0(y) \quad & \text{for } 0 \le y \le 1/2, \\ f(0, y) = 1 \quad & \text{for } 0 \le y < y_i, \\ f(0, y) = 0 \quad & \text{for } y_i \le y < 1, \\ \psi_x(1, y) = \chi_x(1, y) = K_x(1, y) = 0,\ f_x(1, y) = \text{e.s.t.} \quad & \text{for } 0 \le y \le 1/2. \end{aligned} \tag{16}$$

3. The asymptotic solution

In the absence of viscosity the base flow is columnar, *i.e.*, $u = 0$, $w = w_0(y)$ and $K = \omega K_0(y)$, while the mixture fraction distribution is given by the Burke-Schumann solution $f = f_{\mathrm{BS}}(x, y)$, defined below in (31). In this reference state there is no interaction between swirl and reaction. For small swirl levels, departures from the columnar state induced by viscosity are correspondingly small, and as a result, so is the perturbation to the reaction-sheet location. However, as the swirl level increases towards the critical level for breakdown, ω_c, changes in the flow become more pronounced and correspondingly larger perturbations in the reaction-sheet location, resulting from a nonlinear interaction, are anticipated. The following asymptotic analysis, based on the distinguished limit $\Delta\omega \equiv \omega - \omega_c = \mathcal{O}(\sqrt{x_0/\mathrm{Re}})$ derived in [19], estimates these changes. We postulate the asymptotic expansions

$$\begin{aligned} \psi(x, y) &= \psi_0(y) + \epsilon_1 \psi_1(x, y) + \epsilon_2 \psi_2(x, y) + \cdots, \\ K(x, y) &= K_0(y) + \epsilon_1 K_1(x, y) + \epsilon_2 K_2(x, y) + \cdots, \\ \chi(x, y) &= \chi_0(y) + \epsilon_1 \chi_1(x, y) + \epsilon_2 \chi_2(x, y) + \cdots, \\ f(x, y) &= f_{\mathrm{BS}}(x, y) + \epsilon_1 f_1(x, y) + \cdots, \end{aligned} \tag{17}$$

where $\epsilon_1 = \mathcal{O}(\Delta\omega)$ and $\epsilon_2 = \mathcal{O}(\epsilon_1^2)$. Following the analysis of Wang and Rusak [19] one finds the leading-order corrections to the flow to be

$$\psi_1(x, y) \equiv \psi_{1_c}(x, y) = \Phi(y) \sin(\pi x/2),$$

$$K_1(x, y) = \frac{K_{0_y}}{\psi_{0_y}} \psi_1(x, y), \tag{18}$$

$$\chi_1 = -\left(\psi_{1_{yy}} + \frac{\psi_{1_{xx}}}{2x_0^2 y} \right). \tag{19}$$

The quantities Φ and $\Omega_c \equiv \omega_c^2$ are found from the solution of the eigenvalue problem

$$\Phi_{yy} + \left(\Omega_c \frac{\tilde{K}_0 \tilde{K}_{0_y}}{2y^2 w_0^2} - \frac{w_{0_{yy}}}{w_0} - \frac{\pi^2}{8x_0^2 y} \right) \Phi = 0, \quad \Phi(0) = \Phi(1/2) = 0, \tag{20}$$

where $\tilde{K}_0 \equiv K_0/\omega$.

The size of ϵ_1 is determined from the analysis of the second-order terms. Again, details are similar to those in [19] and we obtain the result

$$\epsilon_1^2 M_1 - \epsilon_1 \Delta\Omega M_2 + \frac{x_0}{\mathrm{Re}} M_3 = 0. \tag{21}$$

Here $\Delta\Omega \equiv \Omega - \Omega_c$ with $|\Delta\Omega|/\Omega_c \ll 1$, and

$$M_1 = \frac{4}{3\pi} N_1, \quad M_2 = \frac{1}{2} N_2, \quad M_3 = \frac{4}{\pi^2} N_3, \tag{22}$$

where

$$\begin{aligned} N_1 &= \int_0^{1/2} \left[\frac{\Omega_c}{y w_0^{3/2}} \left(\frac{\tilde{K}_0 \tilde{K}_{0_y}}{y w_0^{3/2}} \right)_y - \frac{1}{w_0} \left(\frac{w_{0_{yy}}}{w_0} \right)_y \right] \frac{\Phi^3(y)}{2} \, \mathrm{d}y, \\ N_2 &= \int_0^{1/2} \frac{\tilde{K}_0 \tilde{K}_{0_y}}{2y^2 w_0^2} \Phi_y^2(y) \, \mathrm{d}y, \\ N_3 &= -2 \int_0^{1/2} \left[\Omega_c \frac{\tilde{K}_0 \tilde{K}_{0_{yy}}}{2y w_0^2} - \frac{y w_{0_{yyy}} + 2 w_{0_{yy}}}{w_0} \right] \Phi(y) \, \mathrm{d}y. \end{aligned} \tag{23}$$

Equation (21) determines ϵ_1 as a function of the parameters $\Delta\Omega$ and x_0/Re. It has a real solution if and only if the following inequality between these parameters holds.

$$|\Delta\Omega| \le \frac{16}{\sqrt{3\pi^3}} \frac{\sqrt{N_1 N_3}}{N_2} \sqrt{\frac{x_0}{\mathrm{Re}}}. \tag{24}$$

When this condition is violated, Equation (21) has no solution, indicating that no steady and near-columnar viscous solution exists close to the critical state. When the condition does hold, we obtain the solutions

$$\epsilon_1\left(x_0/\mathrm{Re}, \Delta\Omega\right) = \frac{3\pi}{8N_1} \left[\frac{\Delta\Omega N_2}{2} \pm \sqrt{\left(\frac{\Delta\Omega N_2}{2} \right)^2 - \frac{64}{3\pi^3} \frac{x_0}{\mathrm{Re}} N_1 N_3} \right]. \tag{25}$$

When (24) holds as an equality, we obtain the fold points, or limit points, of the bifurcation as

$$\omega_{c1}^2 \equiv \Omega_{c1} = \Omega_c - \frac{16}{\sqrt{3\pi^3}} \frac{\sqrt{N_1 N_3}}{N_2} \sqrt{\frac{x_0}{\mathrm{Re}}}, \tag{26}$$

$$\omega_{c2}^2 \equiv \Omega_{c2} = \Omega_c + \frac{16}{\sqrt{3\pi^3}} \frac{\sqrt{N_1 N_3}}{N_2} \sqrt{\frac{x_0}{\mathrm{Re}}}. \tag{27}$$

With ϵ_1 determined, the expansions for the stream function ψ and the axial speed w, correct to first order, can be written as

$$\psi(x, y) \sim \psi_0(y) + \frac{3\pi}{8N_1} \left[\frac{\Delta\Omega N_2}{2} \pm \sqrt{\left(\frac{\Delta\Omega N_2}{2} \right)^2 - \frac{64}{3\pi^3} \frac{x_0}{\mathrm{Re}} N_1 N_3} \right] \Phi(y) \sin(\pi x/2), \tag{28}$$

$$w(x, y) \sim w_0(y) + \frac{3\pi}{8N_1} \left[\frac{\Delta\Omega N_2}{2} \pm \sqrt{\left(\frac{\Delta\Omega N_2}{2} \right)^2 - \frac{64}{3\pi^3} \frac{x_0}{\mathrm{Re}} N_1 N_3} \right] \Phi_y(y) \sin(\pi x/2). \tag{29}$$

With swirl-induced correction to the flow determined, we now turn attention to the expansion for f in the set (17). The leading term of the expansion is the Burke-Schumann term, which satisfies the leading-order version of the species equation (5),

$$w_0 \frac{\partial f_{\mathrm{BS}}}{\partial x} = \frac{x_0}{\mathrm{Pe}} \frac{\partial}{\partial y}\left(2y \frac{\partial f_{\mathrm{BS}}}{\partial y}\right), \tag{30}$$

in which axial diffusion does not come into play. The relevant boundary conditions, provided by (16), are

$$f_{\mathrm{BS}}(0, y) = \begin{cases} 1: & 0 \le y < y_i, \\ 0: & y_i < y \le 1/2, \end{cases}$$

$$f_{\mathrm{BS}_x}(1, y) = \text{e.s.t.} \quad \text{for } 0 \le y \le 1/2,$$
$$f_{\mathrm{BS}_y}(x, 0) = f_{\mathrm{BS}_y}(x, 1/2) = 0 \quad \text{for } 0 \le x \le 1.$$

The solution of (28), for $w_0 = 1$ and subject to the above boundary conditions, is

$$f_{\mathrm{BS}} = f_\infty + \sum_{n=1}^{\infty} B_n J_0(\mu_n \sqrt{2y}) \exp\left(-\frac{\mu_n^2 x_0}{\mathrm{Pe}} x\right), \tag{31}$$

where J_k is the Bessel function of the first kind of order k, μ_n $(n = 1, 2, \dots)$ are the roots of $J_1(\mu_n) = 0$, and

$$f_\infty = 2y_i, \quad B_n = \frac{2\sqrt{2y_i} J_1(\mu_n \sqrt{2y_i})}{\mu_n [J_0(\mu_n)]^2}. \tag{32}$$

The leading-order correction f_1 is found to satisfy the nonhomogeneous equation

$$\frac{\partial f_1}{\partial x} - \frac{x_0}{\mathrm{Pe}} \frac{\partial}{\partial y}\left(2y \frac{\partial f_1}{\partial y}\right) = Q(x, y), \tag{33}$$

where $Q(x, y)$ is a known function, dependent upon the Burke-Schumann solution f_{BS} and the flow correction ψ_1, and given by

$$Q(x, y) = \psi_{1_x} \frac{\partial f_{\mathrm{BS}}}{\partial y} - \psi_{1_y} \frac{\partial f_{\mathrm{BS}}}{\partial x} + \frac{1}{\epsilon_1 \mathrm{Pe}\, x_0} \frac{\partial^2 f_{\mathrm{BS}}}{\partial x^2}. \tag{34}$$

The relevant boundary conditions, obtained from (16), are the homogeneous conditions

$$\begin{aligned} &f_1(0, y) = 0 \quad \text{for } 0 \le y \le 1/2, \\ &f_{1_x}(1, y) = \text{e.s.t.} \quad \text{for } 0 \le y \le 1/2, \\ &f_{1_y}(x, 0) = f_{1_y}(x, 1/2) = 0 \quad \text{for } 0 \le x \le 1. \end{aligned} \tag{35}$$

The solution to the problem for f_1 can be obtained in a straightforward fashion as a series expansion in terms of the eigenfunctions $\phi_n(y) \equiv J_0(\mu_n \sqrt{2y})$ of the associated homogeneous problem

$$2y\phi_n''(y) + 2\phi_n'(y) + \mu_n^2 y = 0, \quad \lim_{y \to 0} \sqrt{y}\phi_n'(y) = 0, \quad \phi_n'(1/2) = 0.$$

The result is

$$f_1 = \sum_{n=1}^{\infty} a_n(x) J_0(\mu_n \sqrt{2y}). \tag{36}$$

Here,

$$a_n(x) = \frac{2}{\left(J_0(\mu_n)\right)^2} \sum_{j=1}^{\infty} B_j \left[-\frac{(\pi/2)\mu_j I_{1jn}}{(\alpha_n - \alpha_j)^2 + \pi^2/4} a_{1jn}(x) + \frac{\alpha_j I_{2jn}}{(\alpha_n - \alpha_j)^2 + \pi^2/4} a_{2jn}(x) + \frac{\alpha_j^2 I_{3jn}}{\epsilon_1 \mathrm{Pe}\, x_0} a_{3jn}(x) \right]. \tag{37}$$

where

$$\alpha_j \equiv \frac{\mu_j x_0}{\mathrm{Pe}}, \tag{38}$$

$$I_{1jn} = \int_0^{1/2} \frac{\Phi(y) J_1(\mu_j \sqrt{2y}) J_0(\mu_n \sqrt{2y})}{\sqrt{2y}}\, \mathrm{d}y, \tag{39}$$

$$I_{2jn} = \int_0^{1/2} \Phi'(y) J_0(\mu_j \sqrt{2y}) J_0(\mu_n \sqrt{2y})\, \mathrm{d}y, \tag{40}$$

$$I_{3jn} = \int_0^{1/2} J_0(\mu_j \sqrt{2y}) J_0(\mu_n \sqrt{2y})\, \mathrm{d}y, \tag{41}$$

and

$$a_{1jn}(x) = -(\alpha_n - \alpha_j)\mathrm{e}^{-\alpha_n x} + \left((\alpha_n - \alpha_j) \cos\frac{\pi x}{2} + \frac{\pi}{2} \sin\frac{\pi x}{2} \right) \mathrm{e}^{-\alpha_j x}, \tag{42}$$

$$a_{2jn}(x) = \frac{\pi}{2}\mathrm{e}^{-\alpha_n x} + \left((\alpha_n - \alpha_j) \sin\frac{\pi x}{2} - \frac{\pi}{2} \cos\frac{\pi x}{2} \right) \mathrm{e}^{-\alpha_j x}, \tag{43}$$

$$a_{3jn}(x) = \frac{\mathrm{e}^{-\alpha_j x} - \mathrm{e}^{-\alpha_n x}}{\alpha_n - \alpha_j}. \tag{44}$$

With f determined to $\mathcal{O}(\epsilon_1)$, we can now compute the corrected location of the reaction sheet. It is found from the expression $f = f_{\mathrm{st}}$, where f_{st} is the stoichiometric value of the mixture fraction, given by

$$f_{\mathrm{st}} = \frac{Y_{O,0}}{\nu Y_{F,0} + Y_{O,0}}. \tag{45}$$

This completes the asymptotic analysis.

4. The numerical solution

To obtain a numerical solution of the governing equations (1–5), subject to the boundary conditions (8–12), a finite-volume method, embodied in the so-called SIMPLER algorithm (see [16] and [29, Sections 6.7 and 6.8] for details) was adopted. We demonstrate the results for the case where the inlet flow is described by the Burgers vortex model,

$$w_0 = 1, \quad v_0 = \frac{1 - \mathrm{e}^{-\beta y}}{\sqrt{2y}}.$$

Here β is a constant related to the vortex core radius, $r_c = 1{\cdot}112/\sqrt{\beta}$. This model is typically used in numerical studies of vortex stability and breakdown of cold flows ([20]–[24]). In the examples presented here we use $\beta = 4$ as a representative case. We first describe solutions of viscous flow in the pipe at various values of x_0/Re, and then the shape of the reaction zone.

To determine the sensitivity of the numerical calculations to axial and radial node spacing, solutions at $\mathrm{Re} = 4000$ with $x_0 = 15$ and various levels of the inlet swirl ω were computed

for two mesh sizes, starting with a basic grid of 550×60 in the axial and radial directions, respectively. Beran and Culick [20] report that the structure and behavior of the breakdown bubble is sensitive to the choice of inflow conditions for the azimuthal vorticity. Therefore, in the present computations, a smaller axial step size was used near the pipe inlet than in the downstream region to increase the computational accuracy of the solution near the inlet. Results for the basic mesh were compared with those for the finer mesh, 750×90.

In keeping with earlier studies ([19], [20]), we use the minimum axial velocity along the pipe axis as a representative measure of the flow state. This quantity represents the largest disturbance in the flow field and when it becomes negative, a vortex breakdown state appears. Figure 1 is a bifurcation diagram that presents the minimum of $w(x, 0)$ as a function of ω for two different meshes. It is seen that mesh refinement produces very close results for values of swirl up to $\omega = 0{\cdot}81$, and the steady solutions are converged. For flows with $\omega > 0{\cdot}81$, in which large-scale vortex zones appear, the finer mesh is needed to capture the breakdown states. Even at this resolution, Figure 1 shows that the computed $w(x, 0)$ does not exhibit full convergence in regions near or within the breakdown zone. Specifically, as the iterations proceed, the solutions exhibit small-amplitude oscillations near the breakdown point. Therefore, most of the computations presented below correspond to flows with swirl levels just below the first appearance of vortex breakdown. Also shown in Figure 1 are results from Beran and Culick [20] for a similar inlet flow in a straight pipe. It can be seen that our computed results agree closely with those in [20] for $\omega > 0{\cdot}78$. At $\omega = 0{\cdot}78$ the first fold occurs in the results of Beran and Culick, followed by a second fold at the secondary limit point $\omega = 0{\cdot}725$ at which a branch of breakdown states emerges for $\omega > 0{\cdot}725$. It should be noted that Beran and Culick do not reports any results on this branch for $\omega > 0{\cdot}73$. These results are in accord with the theory of Wang and Rusak [19], [25], who predict the existence of a two-fold behavior and the appearance of breakdown states when $\omega > 0{\cdot}73$ for $\beta = 4$.

In our computations a hint of the first fold appears at $\omega = 0{\cdot}81$ and breakdown states appear beyond. We clarify that our computational technique, not designed for solution continuation beyond the first fold, is unable to capture solutions along the fold, and the breakdown states in the range $0{\cdot}725 < \omega < 0{\cdot}82$. The comparison with the work of Beran and Culick leads us to conclude that while the present numerical technique accurately computes the flow states up to the first fold point, it loses some accuracy when breakdown zones appear, and although it captures similar qualitative behavior, it cannot access the additional solutions in the range of swirl ratios between the two fold points.

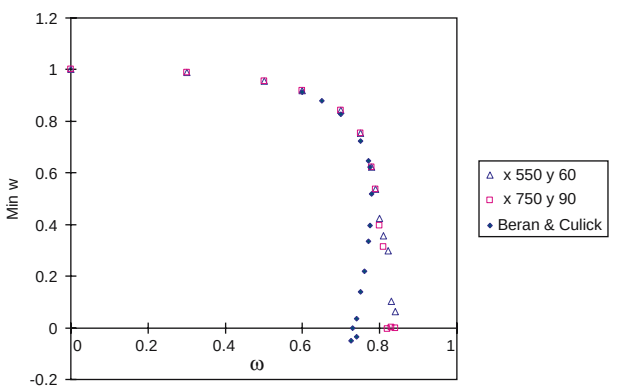

Figure 1. Minimum of axial speed along pipe centerline as function of swirl ratio, for $\mathrm{Re} = 4000$ and $x_0 = 15$.

4.1. Computed examples

Figure 2 shows the values of the minimum axial speed along the pipe centerline and the maximum axial speed along the pipe wall (note that the pipe wall satisfies only a slip boundary condition) as function of the incoming swirl ratio ω for the two cases $\mathrm{Re} = 2000$ and $x_0 = 5$ ($x_0/\mathrm{Re} = 1/400$) and $\mathrm{Re} = 4000$ and $x_0 = 5$ ($x_0/\mathrm{Re} = 1/800$). These computations use the finer mesh mentioned above. Note that for relatively shorter pipes, the axial diffusion terms in the momentum equations have more influence than in much longer pipes. The asymptotic results describe the nonuniqueness of solutions and a fold behavior over certain ranges of the swirl ratio at near-critical swirl levels. This is in agreement with the numerical simulations of Beran and Culick [20]. Our numerical results present a unique solution for each value of ω but exhibit very rapid changes in structure at near-critical swirl ratios as well as at the appearance of vortex breakdown, similar to what was found in Figure 1. It can be seen that the upper branch of the asymptotic results (with the + sign in Equation (29)) shows agreement with results of the numerical simulations, specifically as the ratio x_0/Re is decreased. Also, the asymptotic value of the limit swirl ratio where the fold occurs, ω_{c1}, is close to the numerical value of the swirl ratio where vortex breakdown appears for the first time as ω is increased.

Figures 3(a–d) present the axial velocity distributions along the pipe centerline and wall for $x_0/\mathrm{Re} = 1/800$ and for several near-critical swirl ratios. As the swirl ratio is increased towards the critical, flow perturbations from the columnar solution increase. It can be seen that over a range of swirl levels not very close to the fold point the asymptotic solutions given by (29) show a good correlation with the numerical results all along the pipe axis. For higher levels of swirl the flow exhibits large perturbations and vortex breakdown, and then, the asymptotic approach is not valid.

We now present results for the numerically computed reaction zones. Note that in this diffusive-reactive system, most of the reaction occurs in a narrow zone that is approximated as a surface. The reaction-sheet model assumes that the chemical-reaction time is much shorter than the diffusion time of species and that the reaction only occurs on the interface between fuel and air. Therefore, the reaction sheet can be identified as the surface along which the mixture mass fraction has a stoichiometric value. We consider two reaction states with swirl in the examples below. In the first case the ratio of fuel-to-air radii at inlet is $R_i = 1/6$. Then, the inlet mixture mass fraction has a value less than stoichiometric and the mixture is lean.

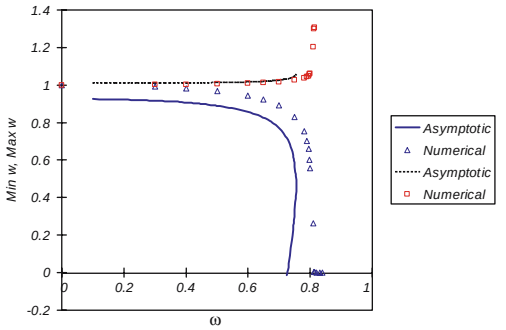

Figure 2a. Minimum of axial speed along pipe centerline (full line for asymptotic solution and open triangles for numerical solution) and maximum of axial speed along pipe wall (dashed line for asymptotic solution and open circles for numerical solution) as a function of swirl ratio. $\mathrm{Re} = 2000$ and $x_0 = 5$.

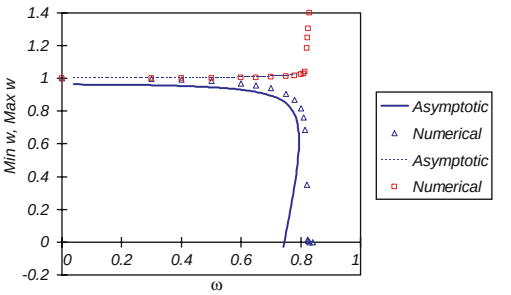

Figure 2b. Minimum of axial speed along pipe centerline (full line for asymptotic solution and open triangles for numerical solution) and maximum of axial speed along pipe wall (dashed line for asymptotic solution and open circles for numerical solution) as a function of swirl ratio. $\mathrm{Re} = 4000$ and $x_0 = 5$.

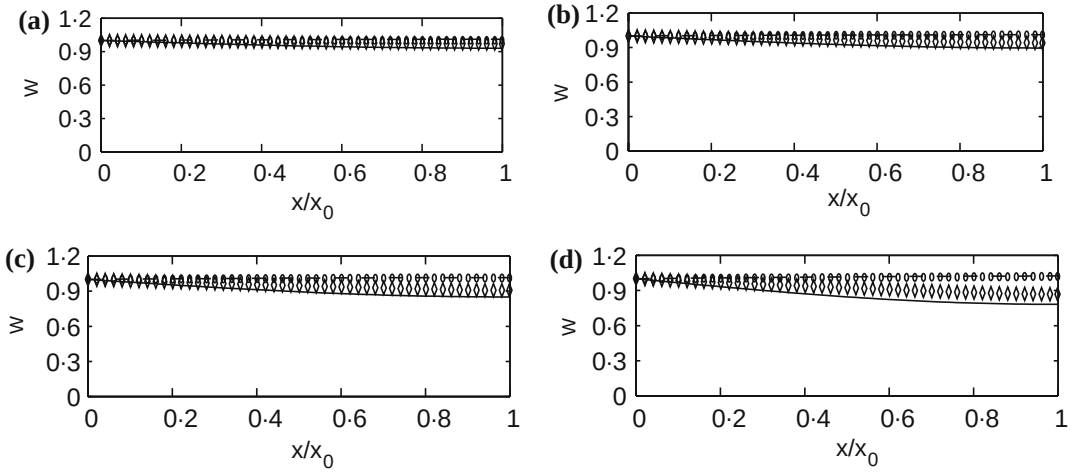

Figure 3. The axial velocity along the pipe centerline (asymptotic results ___, numerical results ◇) and wall (asymptotic results − − − and numerical results ○) for $x_0/\mathrm{Re} = 1/800$ ($\mathrm{Re} = 4000, x_0 = 5$) at (a) $\omega = 0{\cdot}60$, (b) $\omega = 0{\cdot}70$, (c) $\omega = 0{\cdot}75$, (d) $\omega = 0{\cdot}78$.

This condition results in an over-ventilated reaction sheet that closes at the pipe axis. The second case considers a rich mixture, where we take $R_i = 1/4$. This condition results in an under-ventilated reaction sheet which connects to the pipe wall. We consider these reaction states for a variety of values of Pe.

Figures 4 and 5 display the length of the reaction zone as a function of swirl ratio ω for both over-ventilated and under-ventilated cases and for various values of Pe. These figures show a comparison of asymptotic results from Equations (17), (31) and (36) with numerical results, for $x_0/\mathrm{Re} = 1/400$ and $x_0/\mathrm{Re} = 1/800$. The agreement is good for swirl ratios up to the limiting level ω_{c1} defined in (26). It can be seen that the flame length is slightly reduced as the swirl ratio is increased towards the limit level for both the over- and under-ventilated cases. The numerical solutions display further changes in the length of the reaction zone as vortex-breakdown states appear.

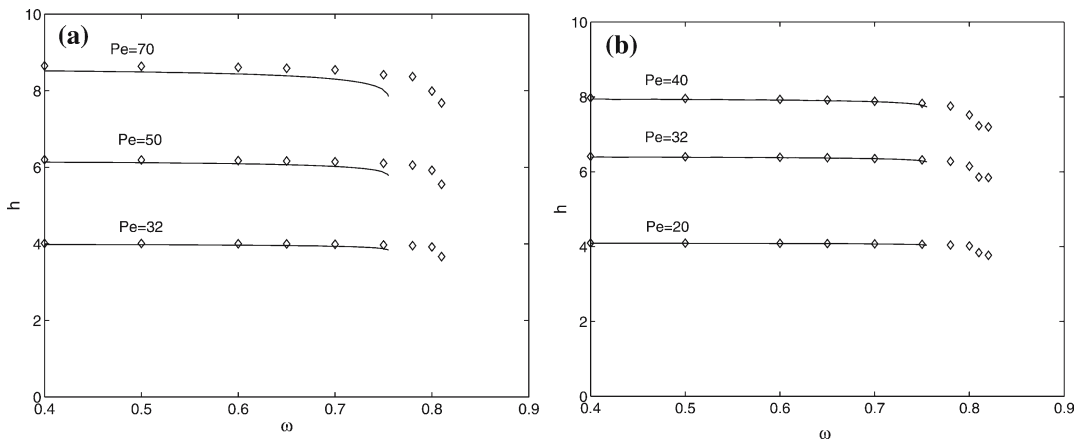

Figure 4. Comparison of asymptotic results (−) and numerical simulations (◇) for length of reaction zone, at $x_0/\mathrm{Re} = 1/400$ ($\mathrm{Re} = 4000, x_0 = 10$): (a) over-ventilated (b) under-ventilated.

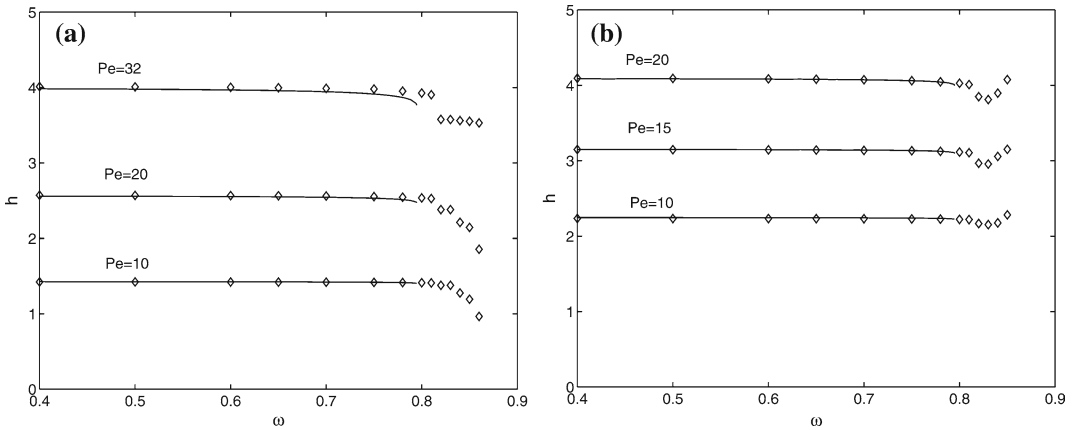

Figure 5. Comparison of asymptotic results (−) and numerical simulations (◇) for length of reaction zone, at $x_0/\mathrm{Re} = 1/800$ ($\mathrm{Re} = 4000, x_0 = 5$): (a) over-ventilated (b) under-ventilated.

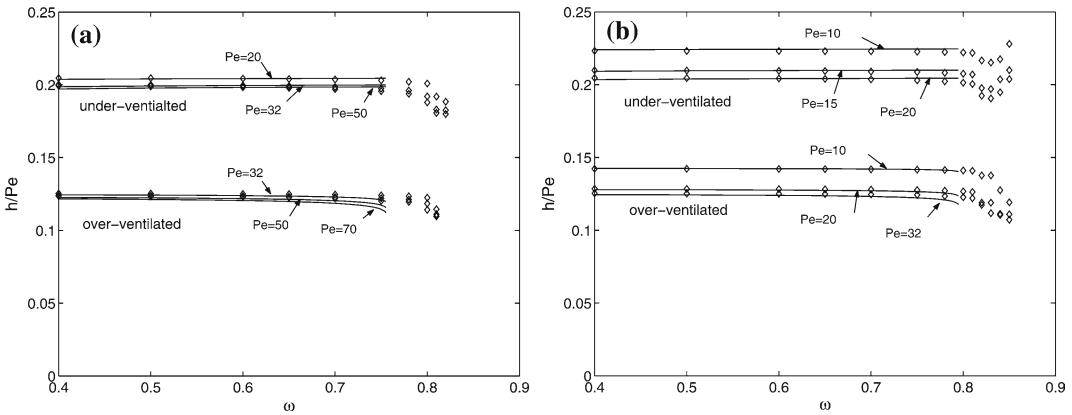

Figure 6. Scaled reaction-zone length h/Pe against swirl ratio ω according to asymptotic results (−) and numerical calculations (◇) for: (a) $x_0/\mathrm{Re} = 1/400$ ($\mathrm{Re} = 4000, x_0 = 10$), (b) $x_0/\mathrm{Re} = 1/800$ ($\mathrm{Re} = 4000, x_0 = 5$).

Figure 6 shows the scaled reaction-zone length h/Pe as a function of the swirl ratio for both over- and under-ventilated cases. This parameter comes from the exponential term of the Burke-Schumann solution, Equation (31). Results are again presented for $x_0/\mathrm{Re} = 1/400$ and $x_0/Re = 1/800$. It is seen that when Pe is sufficiently high, the value of the scaled reaction-zone length is nearly constant for swirl ratios up to the limit swirl level: $h/\mathrm{Pe} \sim 0{\cdot}125$ for the over-ventilated case (with $R_i = 1/6$) and $h/\mathrm{Pe} \sim 0{\cdot}21$ for the under-ventilated case (with $R_i = 1/4$). These values change as the incoming swirl ratio is further increased and vortex breakdown zones appear in the flow. Then, the flow and reaction-zone behavior are much more nonlinear and cannot be predicted by the present asymptotic approach.

Figure 7 illustrates the effect of x_0/Re on the scaled reaction-zone length according to the asymptotic analysis. We can see that as the flow perturbation increases with the decrease of x_0/Re, the reaction-zone length is decreased. Note, however, that the present analysis is limited to small values of x_0/Re and when this parameter increases above $1/200$ the asymptotic results are no longer accurate.

Figure 8 shows a comparison between the asymptotic and computational results for the over- and under-ventilated reaction-zone shapes at $x_0/\mathrm{Re} = 1/800$ and various near-critical

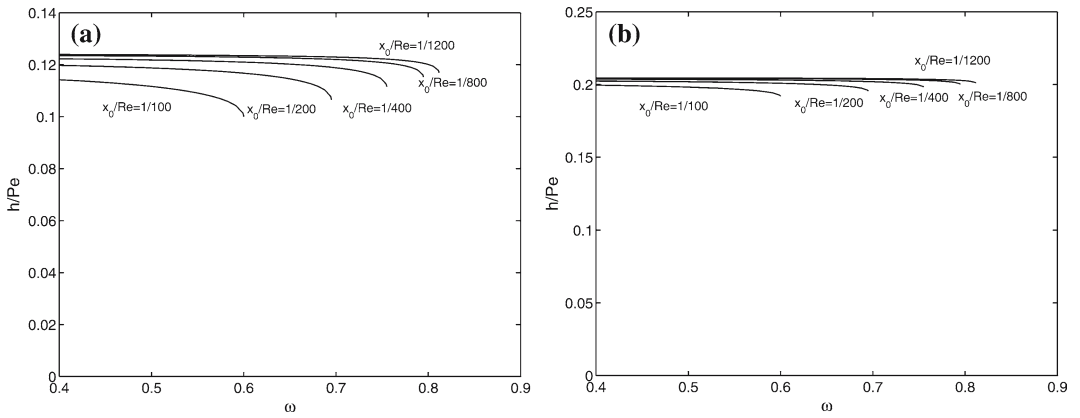

Figure 7. The effect of x_0/Re on scaled reaction-zone length according to the asymptotic solutions: (a) over-ventilated with $x_0/\mathrm{Pe} = 5/40$, (b) under-ventilated with $x_0/\mathrm{Pe} = 5/20$.

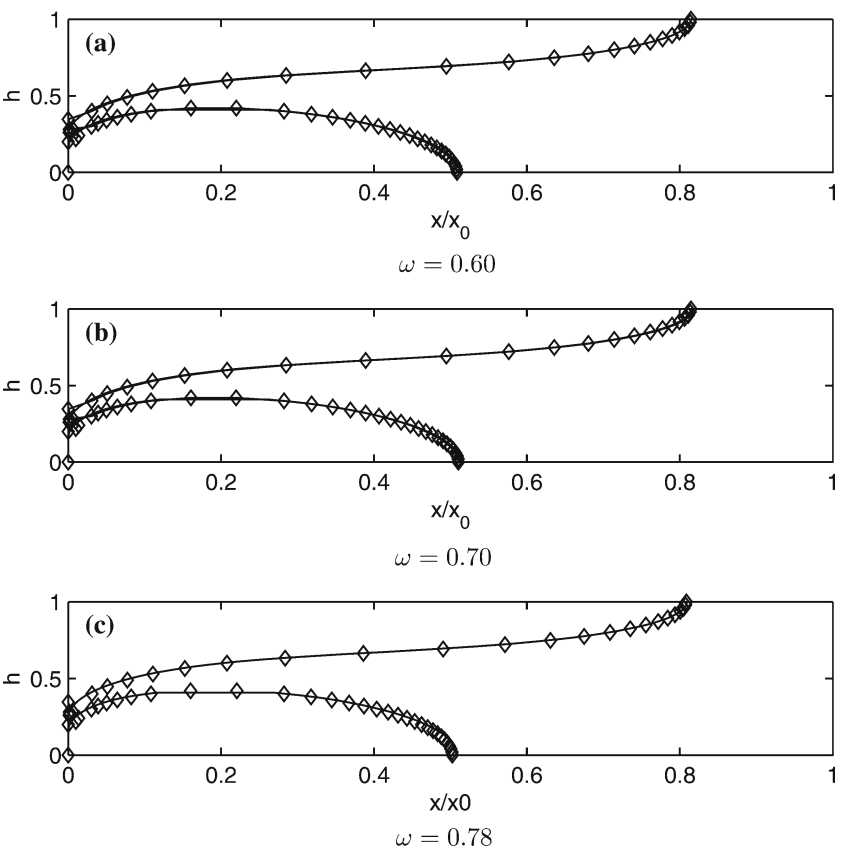

Figure 8. Comparison of reaction-zone shapes from asymptotic results (−) and numerical calculations (◊) at $x_0/\mathrm{Re} = 1/800$ ($\mathrm{Re} = 4000, x_0 = 5$) and $\mathrm{Pe} = 20$.

swirl levels. The predicted shape of the reaction-zone according to the asymptotic solution is close to that computed by the numerical simulation for swirl range below critical.

Figure 9 is a computational exploration of the influence of increase in swirl on streamline patterns and reaction-zone shapes for both under- and over-ventilated cases. Representative results are presented for $x_0 = 5$, $\mathrm{Re} = 4000$ and $\mathrm{Pe} = 20$. Computations show that the nearly

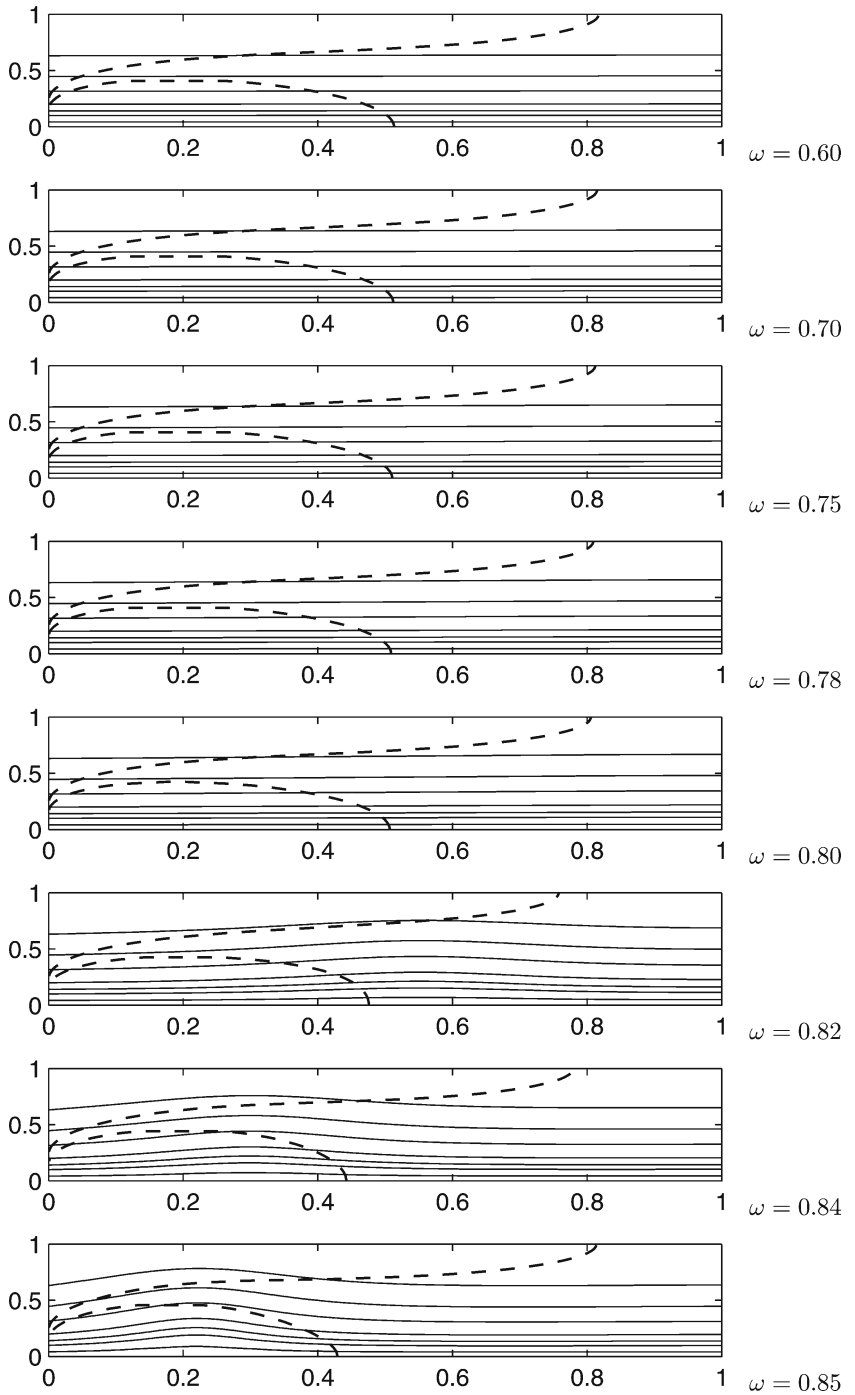

Figure 9. Streamlines pattern and flame shape from numerical results for several swirl ratios at $x_0/\mathrm{Re} = 1/800$ ($\mathrm{Re} = 4000$, $x_0 = 5$) and $\mathrm{Pe} = 20$.

columnar flow is significantly disturbed as swirl is increased. A vortex breakdown (reversed flow) zone near the pipe centerline appears when the swirl ratio is above the limit level, at $\omega =$ 0·82. The breakdown zone moves upstream as swirl is increased further. Before breakdown, reaction-zone length decreases with increase in swirl for both over- and under-ventilated

cases. As the breakdown zone appears and increases in size, the over-ventilated reaction zone becomes axially shorter and compact, while expanding radially. On the other hand, the under-ventilated reaction zone becomes longer and narrower.

These changes in the reaction zone shape are directly related to changes in the flow pattern as the incoming swirl ratio is increased. Deceleration of the axial flow and the development of an outward radial flow near the centerline influence the size of the over-ventilated reaction zone and cause it to become shorter and expand radially as swirl is increased. This effect is even more pronounced when vortex breakdown zones appear. On the other hand, the development of an outward radial flow near the wall influences the size of the under-ventilated reaction zone and makes it shorter as swirl is increased toward the limit level. When vortex breakdown zones appear, the accelerated flow near the wall causes an increase in the under-ventilated reaction-zone length.

5. Conclusions

The effect of near-critical swirling flow on the structure of the classical Burke-Schumann reaction sheet is investigated by asymptotic analysis and numerical computation. It is found that in high-Reynolds-number flows the swirl-induced change from the columnar state can be described by a nonlinear reduced-order model, as in the work of Wang and Rusak [19]. These flow changes are used to calculate the corrections due to swirl to the classical diffusion-reaction structure according to the Burke-Schumann solution. The resulting corrections apply to both lean and rich conditions of reaction. The asymptotic results show good agreement with numerical simulations, specifically as the Reynolds number is increased and $\omega < \omega_{c1}$. the numerical results extend the investigation into regions where the asymptotic analysis is not valid.

It is found that as swirl is increased towards the critical level, the flow decelerates near the chamber centerline, accelerates near the chamber wall, and a field of outward radial speed develops. For sufficiently high levels of swirl a large separation zone (near stagnation breakdown) appears around the centerline, the leading point of which shifts toward the pipe inlet as swirl is further increased. As a result, in the case of lean reaction, the reaction-sheet shortens in length, expands laterally, and becomes more compact. On the other hand, the flow changes near the wall as swirl is increased result in nonlinear changes in the length of the rich reaction sheet. When the swirl is below the limit level the reaction zone becomes shorter, but as breakdown appears the rich reaction zone becomes narrower but longer. This work extends the Burke-Schumann reaction-sheet theory to include the effect of swirl.

Acknowledgements

This research was supported by the National Science Foundation under Grant No. CTS-9904327.

References

1. S.P. Burke and T.E. Schumann, Diffusion flames. *Industr. Engng. Chem.* 20 (1928) 998–1004.
2. F.A. Williams, *Combustion Theory*. Menlo Park, California: Benjamin Cummings (1985) 680 pp.
3. F.G. Roper, The prediction of laminar jet diffusion flame sizes: part I. Theoretical model. *Combust. Flame* 29 (1977) 219–226.
4. F.G. Roper, C. Smith and A.C. Cunningham, The prediction of laminar jet diffusion flame sizes: part II. Experimental verification. *Combust. Flame* 29 (1977) 227–234.

5. M. Klajan and A.K. Oppenheim, Influence of exothermicity on the shape of a diffusion flame. In: *19th Symposium (International) on Combustion*. The Combution Institute, Pittsburgh, Pennsylvania (1982) pp. 223–235.
6. S.H. Chung and C.K. Law, Burke-Schumann flame with streamwise and preferential diffusion. *Combust. Sci. Technol*. 37 (1984) 21–46.
7. S.C. Li, A.S. Gordon and F.A. Williams, A simplified method for computation of Burke-Schumann flames in infinite atmospheres. *Combust. Sci. Technol.* 104 (1995) 75–91.
8. A.K. Gupta, D.G. Lilley and N. Syred, *Swirl Flows*, Tunbridge Wells, Kent, UK: Abacus Press (1984) 476 pp.
9. A.W. Marshall and A.K. Gupta, Effects of jet momentum on thermal characteristics of co-swirling flames. *AIAA paper 96-0404* (1996).
10. A.H. Lefebvre, *Gas Turbine Combustion*, 2nd Edition. Philadelphia: Taylor and Francis (1999) 400 pp.
11. J.R. Stephens, S. Acharya and E.J. Gutmark, Controlled swirl-stabilized spray combustor. *AIAA paper 97-0464* (1997).
12. M.S. Cha, D.S. Lee and S.H. Chung, Effect of swirl on lifted flame characteristics in nonpremixed jets. *Combust. Flame* 117 (1999) 636–645.
13. E.E. Khalil, D.B. Spalding and J.H. Whitelaw, The calculation of local flow properties in a two-dimensional furnace. *Int. J. Heat Mass Transfer* 18 (1975) 775–791.
14. S.E. Elgobashi, *Characteristics of Gaseous Turbulent Diffusion Flames in a Cylindrical Furnace*. Ph.D. Thesis, London University (1974).
15. M.A. Habib and J.H. Whitelaw, Velocity characteristics of confined coaxial jets with and without swirl. *J. Fluids Engng*. 102 (1980) 44–53.
16. S.Y. Shim, K.H. Sohn and C.S. Lee, A study of the combustion characteristics of coaxial jet furnaces with swirl flow. *KSME J*. 7 (1993) 389–398.
17. Z. Rusak, A.K. Kapila and J.J. Choi, Effect of combustion on near-critical swirling flow. *Combust. Theory Modell*. 6 (2002) 625–646.
18. K.H. Sohn, *Nonpremixed Combustion With Swirl*. PhD Thesis, Rensselaer Polytechnic Institute, Troy, New York (2004).
19. S. Wang and Z. Rusak, The effect of slight viscosity on a near-critical swirling flow in a pipe. *Phys. Fluids* 9 (1997) 1914–1927.
20. P.S. Beran and F.E.C. Culick, The role of nonuniqueness in the development of vortex breakdown in tubes. *J. Fluid Mech*. 242 (1992) 491–527.
21. P.S. Beran, The time-asymptotic behavior of vortex breakdown in tubes. *Comp. Fluids* 23 (1994) 913–937.
22. J.M. Lopez, On the bifurcation structure of axisymmetric vortex breakdown in a constricted pipe. *Phys. Fluids* 6 (1994) 3683–3693.
23. K.K. Kuo, *Principles of Combustion*. New York: John Wiley & Sons (1986) 810 pp.
24. Z. Rusak, S. Wang and C.H. Whiting, The evolution of a perturbed vortex in a pipe to axisymmetric vortex breakdown. *J. Fluid Mech.* 366 (1998) 211–237.
25. S. Wang and Z. Rusak, The dynamics of a swirling flow in a pipe and transition to axisymmetric vortex breakdown. *J. Fluid Mech*. 340 (1997) 177–223.
26. C. Bruecker and W. Althaus, Study of vortex breakdown by particle tracking velocimetry (PTV), part 3. Time dependent structure and development of breakdown modes. *Experiments in Fluids* 18 (1995) 174–186.
27. E. Malkiel, E. J. Cohen, Z. Rusak and S. Wang, Axisymmetric vortex breakdown in a pipe – theoretical and experimental studies. In: *36th Israel Annual Conference on Aerospace Sciences*. Tel-Aviv, Israel (1996) pp. 24–35.
28. T.W. Mattner, P.N. Joubert and M.S. Chong, Vortical flow. Part 1. Flow through a constant-diameter pipe. *J. Fluid Mech*. 463 (2002) 259–291.
29. S.V. Patankar, *Numerical Heat Transfer and Fluid Flow*. Washington, D.C.: Hemisphere (1980) 197 pp.